Volume-of-interest CT imaging with dynamic beam filtering using multiple aperture devices

Wenying Wang, Grace J. Gang, Andrew Mao, Alejandro Sisniega, Jeffrey H. Siewerdsen, and J. Webster Stayman
Department of Biomedical Engineering, Johns Hopkins University, Baltimore MD, USA 21205

***Abstract*—Interior tomography is promising approach for retaining high quality CT images within a volume-of-interest (VOI) while reducing the total patient dose. A static collimating filter can only image a centered symmetric VOI, which requires careful patient positioning and may be suboptimal for many clinical applications. Multiple aperture devices (MADs) are an emerging technology based on sequential binary filters that can provide a wide range of fluence patterns that may be adjusted dynamically with relatively small motions. In this work, we introduce a general approach for VOI imaging using MAD-based fluence field modulation (FFM). Physical experiments using a CT test bench are conducted illustrating off-center x-ray beam control for imaging the spine in an abdominal phantom. Image quality and dose metrics are computed for both standard full-field CT and VOI CT. We find that the image quality within the VOI can be preserved for VOI CT with a significant drop in integral dose as compared with a standard full-field protocol.**

I. INTRODUCTION

X-ray CT is widely used for diagnosis, disease monitoring, and in interventional procedures. However, increased usage has raised concern about excessive radiation exposure. In many CT applications, only a limited volume is required for assessment. For example, target positions are generally known in single-organ studies (e.g. cardiac imaging) and in interventional procedures focused on particular sites (e.g. spine imaging). Despite the need for only local structural information, CT scans routinely cover the entire lateral extent of the patient. Volume-of-interest (VOI) scanning gives the opportunity to spare dose to surrounding tissues, while providing the information required inside the VOI [1].

Implementing VOI imaging can be challenging for arbitrary VOIs. Many VOI studies have used static collimation to restrict the X-ray beam width [2], or static zonal filtering to decrease the fluence intensity outside the VOI [3]. However, these methods can only collect centered, cylindrical VOIs (using standard source-detector trajectories) limiting practical application. Several attempts have been made to increase versatility in VOI imaging. Kolditz *et al.* took advantage of mobility of C-arm CT system and realized non-centered VOI imaging [4]; and dynamic collimation has been applied to achieve adaptable fluence patterns with off-centered VOIs. [5]

In previous work, we introduced a novel filtering scheme using fine-scale binary filters called multiple aperture devices (MADs) [6]. In this scheme, two MADs are used in series. Translations of the dual-MAD filtering system as a whole shifts the peak of the incident beam and small relative displacements between two components changes the width of transverse fluence profile. This new filtering system provides the capability for sophisticated fluence-field modulation (FFM) based on the specific imaging task. In this work, we present a dual-MAD trajectory design for an arbitrary VOI imaging task. VOI CT acquisition is conducted on a CT bench and truncated projection data are reconstructed using an extrapolation-based method. Image quality and dose are assessed for both standard full-field CT and MAD-based VOI CT. Dose is estimated using Monte Carlo simulation, bare-beam fluence measurements, and an estimated phantom density map.

II. MATERIALS AND METHODS

A. Filter Trajectory Design for arbitrary VOI

MADs-based FFM provides much flexibility for general VOI imaging. We will describe the desired VOI using a 3D binary mask, m_{VOI}, where voxels within the VOI have value 1, and outside the VOI are 0. Furthermore, let $m_{\text{VOI}} \in \mathbb{R}^N$ be a column vector with N denoting the total number of voxels in a full-field image volume. At each projection angle θ, a detector pixel mask associated with the VOI projection area is

$$g(\theta) = \Theta\{\mathbf{A}(\theta) m_{\text{VOI}} > 0\} \tag{1}$$

where $\mathbf{A}(\theta) \in \mathbb{R}^{P \times N}$ is the system matrix at projection angle θ (with P being the total number of pixels on detector.) The logical operator, $\Theta\{\cdot\}$, returns 1 if the argument is true and 0 if false. Thus, $g(\theta) \in \mathbb{R}^P$ is the binary mask describing the data required to reconstruct the VOI. (We note that such data is not generally mathematically complete [7].)

Current MAD-based FFM has focused only on modulation of the X-ray beam in the transverse direction (along the detector). We denote $g(\theta)$ reshaped to a 2D mask corresponding to the face of the detector as $G_\theta(u,v) \in \mathbb{R}^{U \times V}$ (where u and v are detector coordinates in the transverse and transaxial directions, respectively; U/V denote the number of detector column/rows on the detector panel; and $P = U \times V$). Thus all column indices required for obtaining a desired VOI (illustrated in Fig. 1) may be written as

$$\{u_{\text{VOI}}\}(\theta) = \{u | \textstyle\sum_v G_\theta(u,v) > 0\}. \tag{2}$$

To find the optimal actuation of MAD filters for VOI imaging, we consider two requirements: 1) Maximize the fraction of fluence transmitting through VOI region. And, 2) constrain the minimum filter transmissivity passing through the VOI region to be no less than some threshold f_{min}. (E.g., There is some minimal level of fluence required to obtain useful images in the VOI.) Mathematically, we may then write full FFM objective function as

$$(\hat{t}_0, \hat{t}_1)(\theta) = \arg \max_{(t_0,t_1)\in\mathcal{T}_\theta} \frac{\sum_{u\in\{u_{\text{VOI}}\}(\theta)} f(u;t_0,t_1)}{\sum_u f(u;t_0,t_1)}, \tag{3}$$

$$\mathcal{T}_\theta = \{(t_0,t_1) | \min_{u\in\{u_{\text{VOI}}\}(\theta)} f(u;t_0,t_1) > f_{\text{min}}\}. \tag{4}$$

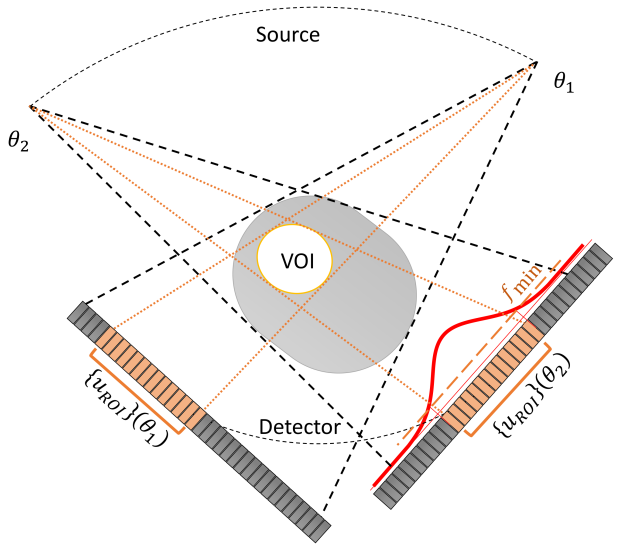

Fig. 1: MAD-based VOI scan diagram and notation: $\{u_{\text{VOI}}\}(\theta)$ is defined as a set of detector indices based on projection of the VOI at each projection angle θ; the incident fluence to $\{u_{\text{VOI}}\}(\theta)$ is constrained to be above f_{min}.

where $f(u;t_0,t_1)$ denotes all fluence field patterns (a function of u) achievable from the dual-MAD system which is controlled through two actuation parameters: t_0, the translation of MAD0, and t_1 the translation of MAD1 relative to MAD0. That is, the parameter pair (t_0,t_1) defines the fluence profile $f(u;t_0,t_1)$ which is determined experimentally through a pre-calibration using an exhaustive sweep through varying (t_0,t_1).

The above optimization is complicated by the periodic nature of $f(u;t_0,t_1)$. That is, the MAD filters themselves are quasi-periodic which means that fluence patterns will repeat for motions on the order of one MAD period. To avoid difficulties in optimization and to enforce actuations with relatively small displacements between two acquisition frames, we make the following modifications. Given a circular orbit, the projection of VOI center may be approximated by a sinusoidal curve. Thus, we perform an initial optimization using (3) and (4) and then perform a sinusoidal fitting $\tilde{t}_0(\theta)$ to $\hat{t}_0(\theta)$. Subsequently, we perform a second optimization, constraining the final displacements $\hat{t}_0^{\text{fit}}$ to be close to the sinusoidal approximation, with

$$(\hat{t}_0^{\text{fit}},\hat{t}_1^{\text{fit}})(\theta)=\arg\max_{(t_0,t_1)\in\mathcal{T}_\theta^{\text{fit}}}\frac{\sum_{u\in\{u_{\text{VOI}}\}(\theta)}f(u;t_0,t_1)}{\sum_u f(u;t_0,t_1)}, \quad (5)$$

$$\mathcal{T}_\theta^{\text{fit}}=\{(t_0,t_1)\in\mathcal{T}_\theta:|\hat{t}_0^{\text{fit}}(\theta)-\tilde{t}_0(\theta)|<\Delta t\}. \quad (6)$$

In our test-bench experiments, we select $f_{\text{min}}=0.2$ and $\Delta t=0.1$ mm (this is small relative to the MAD period of 0.9 mm).

B. Truncated CT reconstruction

Projection data acquired using MAD filters require careful calibration for a number of physical effects. This includes sensitivity to focal spot changes and spectral effects. A modified forward model is employed to account for these effects. Specifically,

$$\bar{y}(\theta)=g_{I_0}g_D g_M(\theta)e^{-\alpha(\theta)l} \quad (7)$$

where g_{I_0} is the emitted X-ray fluence strength distribution, g_D is the detector sensitivity map, and $g_M(\theta)$ is the designed MAD modulation profile (including calibrations for focal spot positioning). To compensate for spectral effects, we estimate a first-order spectral correction term $\alpha(\theta)$ from variable thickness slabs, which may be applied as a data correction (much like ray-based beam hardening corrections). Inverting the above forward model [8], we compute a sinogram $l(u(\theta),v,\theta)$ from noisy measurements y.

Since VOI data is highly truncated, direct FDK reconstructions suffer severe artifacts within the ROI. Here we extrapolate the sinogram along the transverse direction using a quadratic model [9] to alleviate the influence of truncation within the VOI. Specifically, for each line integral profile on the v^{th} row at one projection angle θ, extrapolations are performed on each truncated side independently,

$$l_{\text{ext}}(u)=\alpha(u-u_0(\theta))^2+\beta(u-u_0(\theta))+\gamma \quad (8)$$

where u_0 is the index of the nearest truncation point. Assuming continuity at the truncation point ($u=u_0$) and $l=0$ at the detector boundary $u=u_b$, and we derive

$$\beta(v,\theta)=\frac{\partial l(u,v,\theta)}{\partial u}|_{u=u_0(\theta)}, \quad (9)$$

$$\gamma(v,\theta)=l(u_0(\theta),v,\theta), \quad (10)$$

$$\alpha(v,\theta)=-\frac{\beta(v,\theta)(u_b-u_0(\theta))+\gamma(v,\theta)}{(u_b-u_0(\theta))^2}. \quad (11)$$

With noisy line integral profiles, $\beta(v,\theta)$ and $\gamma(v,\theta)$ are estimated with a local linear regression. Extrapolated line integrals are enforced to be non-negative, and are used as a direct input into a standard FDK algorithm to reconstruct the VOI.

C. Experiment Setup

To investigate the MAD-based VOI imaging feasibility, experiments were conducted on a cone-beam CT test bench with dual MAD filters (Fig. 2a). A circular region around the spine in a QRM abdomen phantom (Fig. 2b) is chosen as the VOI. Note that MAD-based fluence field patterns allow for control of beam width, permitting noncircular VOI.

In addition to MAD-VOI scans, reference "high"-dose and low-dose scans without the MAD filters are acquired for comparison. In each scan, 720 frames are acquired in a single rotation with constant angular steps. Experiments were performed at 100 kVp, 35 mA. For the high-dose and low-dose scans, pulse widths of 18.2 ms and 3.2 ms were used, respectively. This corresponded to an incident fluence, I_0, of 8.1×10^5 photons per pixel and 1.58×10^5 photons per pixel for the high- and low-dose scans, respectively (estimated based on bare-beam variance measurements). MAD-VOI acquisition used the same tube settings as the high-dose scan. After appropriate gain-correction and constant scatter correction (with single scatter-to-primary-ratio tuned to remove the cupping artifact), Feldkamp (FDK) reconstruction was performed with a Hamming window, 0.4 Nyquist frequency cutoff, and a $120\times120\times10$ volume with cubic 0.5 mm voxels.

For MAD-VOI and low-dose experiments, we used Monte-Carlo simulation to estimate the dose distribution. [11] The

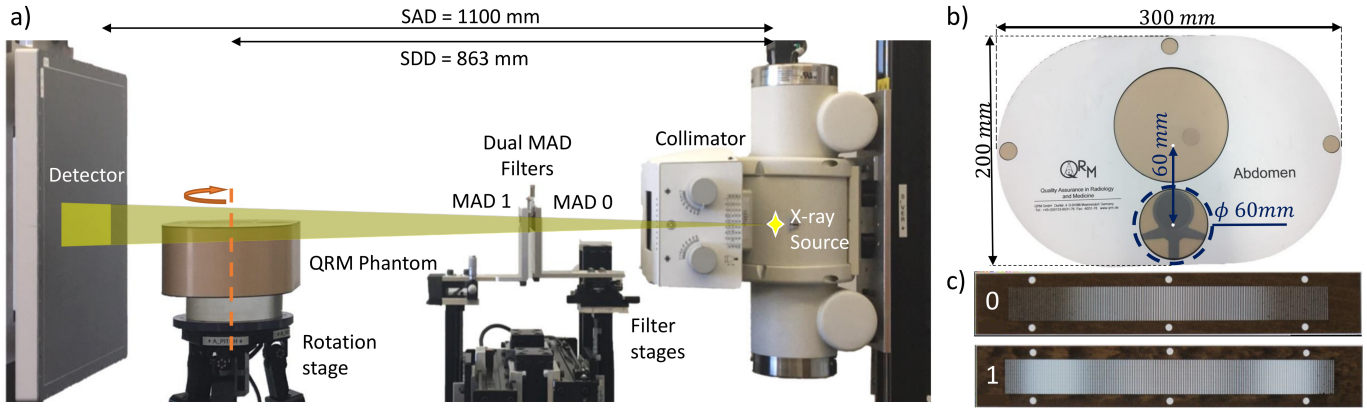

Fig. 2: a) Test bench experiment setup. b) Abdomen QRM phantom. c) Photograph of manufactured dual MADs. [10]

input fluence fields were acquired using bare-beam measurements scaled by the estimated I_0 values. Contrast-to-noise ratios and dose are reported for all three experiments.

III. Results

A. Filter Trajectory Design

The estimated filter trajectory based on the proposed optimization for the spine VOI is shown in Fig. 3a. The blue dashed line shows the MAD0 translations at each projection angle, and the red curve shows the MAD1 translation relative to the MAD0 position. This designed trajectory results in the bare-beam dynamic fluence-field modulation shown in Fig. 3b.

As the long axis of QRM phantom is 300 mm, the full projection data will occupy over 90% of the detector transversely. In contrast, the diameter of the VOI is only 60 mm, ∼1/5 of the long axis size. The designed modulation profile only illuminates ∼1/4 of the detector with filter transmissivity larger than 20% suggesting a good match with the design objective.

The VOI in this study is cylindrical and off-center. Thus, the x-ray beam center is shifted sinusoidally along with the axial center of the VOI. The width of beam is nearly constant over projection angle. Relative translation between the two MADs is required even for constant width designs due to obliquity effects that narrow beam profiles with an off-centered MAD0.

B. Image quality analysis and dose calculation

MAD-VOI was processed according to the modified forward model (7) with extrapolation to approximate a complete sinogram (Fig. 4a). FDK reconstruction of the VOI for full-field high-dose, full-field low-dose, and MAD-VOI scans are shown in Figures 4b, 4c, 4d, respectively. The noise distribution was estimated by computing the standard deviation over 10 (axial) slices and are shown in Figures 4e, 4f, 4g. We observe that the MAD-VOI reconstruction has lower noise than full-field low-dose result, and the CT number bias appears smaller. The MAD-VOI reconstruction has some mild structured noise and ring artifacts. We conjecture that these residual imperfections are due to errors in the MAD gain correction process.

The QRM phantom provides uniform regions in "spinal bone" and "soft tissue" interior to the spine. We computed the contrast-to-noise ratio (CNR) between these two tissues divided by noise in the background.

$$\mathrm{CNR} = \frac{\mu_{\text{bone}} - \mu_{\text{soft-tissue}}}{\sigma_{\text{background}}} \tag{12}$$

The results of the Monte Carlo simulation of dose distribution maps in MAD-VOI and full-field low-dose scans are shown in Fig. 5. In the MAD-VOI scan, the dose is accumulated more highly in the VOI rather than the more even distribution along peripheral tissues in the full-field scan.

CNR, integral dose and dose accumulated exterior to the VOI estimates for all methods are summarized in Table I. Note that the integral dose in MAD-VOI scan is reduced by

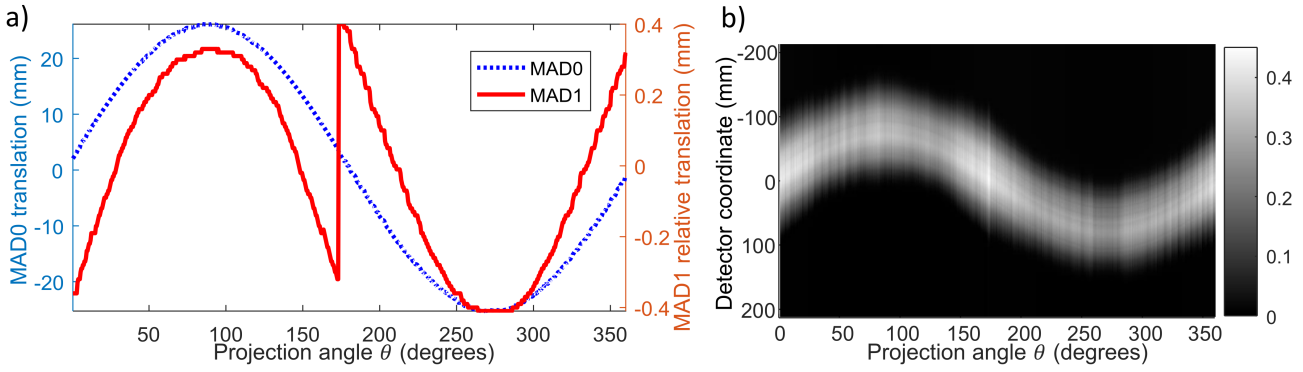

Fig. 3: a) Estimated actuation trajectories for MAD-VOI acquisition. b) Measured bare-beam fluence for the off-center VOI.

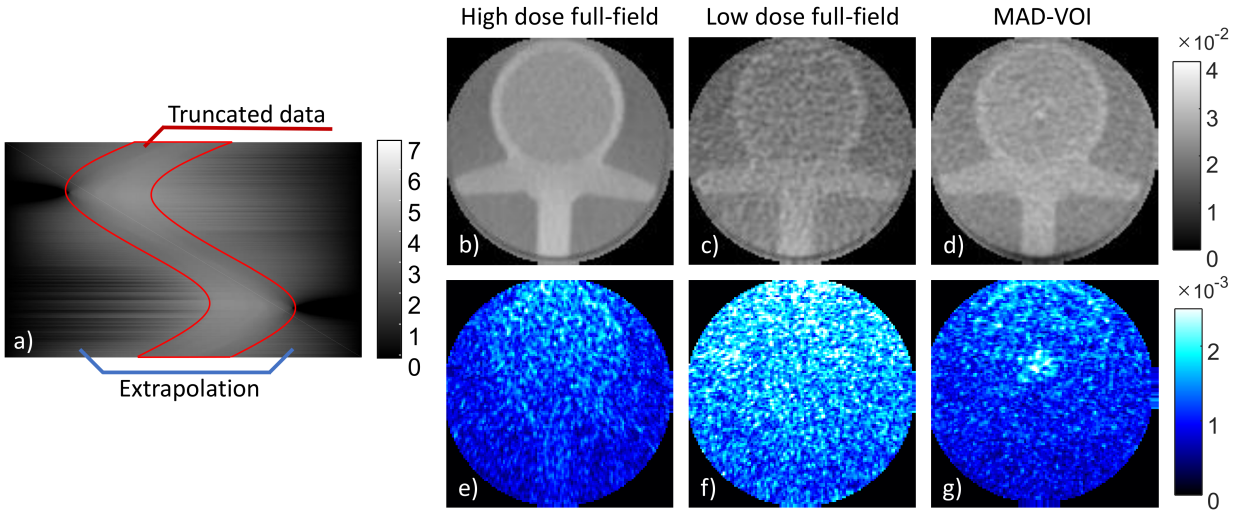

Fig. 4: a) Central slice extrapolated sinogram. The truncated data is marked in red, while the extrapolation region is marked in blue. Upper row: FDK reconstructions of the VOI in the: b) Full-field high-dose scan; c) Full-field low-dose scan; and d) MAD-VOI scan. Bottom row: e)-g): Reconstruction noise based on the standard deviation over 10 slices.

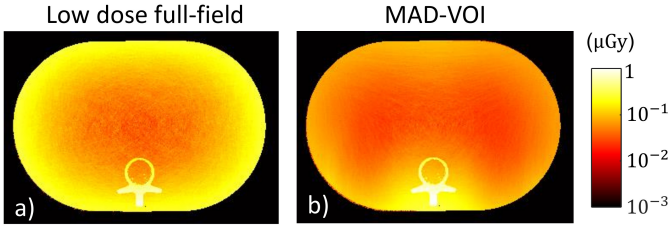

Fig. 5: Absorbed dose distribution in the a) full-field low-dose scan and the b) MAD-VOI scan. For optimal display effect, the colormap is shown in log-scale.

40% while the CNR is not decreasing (as compared with the low-dose scan). Also note that while the (reference) high-dose scan and the MAD-VOI scan used the same x-ray technique, the dual-MAD filter transmissivity peaks around 40% and one should not expect to achieve the same CNR. The comparison between the full-field low-dose and MAD-VOI scans suggests that MAD-VOI has the potential to retain high quality VOI images while reducing integral dose.

TABLE I: CNR and Integral Absorbed Dose

Experiment	CNR	Dose (mGy)		
		Outside VOI	In VOI	Total
High-dose full-field	7.27	29.3	2.87	32.1
Low-dose full-field	2.73	5.71	0.556	6.27
FFM-VOI	2.90	2.72	0.784	3.51

IV. Discussion

In this work, we apply novel MAD-based FFM to VOI CT imaging. These dynamic filters can tailor the beam width and center for non-centered and irregular-shaped VOIs (to be explored additionally in ongoing studies). A preliminary bench-top study on a QRM phantom shows that MAD-VOI imaging retains good image quality while significantly decreasing the integral dose as compared with full-field exposures.

These preliminary studies focused on relatively simple extrapolation-based FDK for truncated data. Future work will employ more sophisticated (e.g., Hilbert-transform methods [7] [12] and model-based reconstruction [13]). Similarly, ongoing studies are considering combination of fluence-field modulation and tube-current modulation for additional control of dose and image quality. Other future work includes the development of new MAD filters for more varied fluence patterns including bimodal beam patterns and profiles that are peaked but non-zero outside a region of interest. Such patterns may facilitate more sophisticated scans including two disconnected VOIs (e.g. lungs, kidneys) and untruncated scans with two dose/image quality levels inside/outside a specified VOI [14].

Acknowledgment

Work was supported, in part, by NIH grant U01EB018758.

References

[1] G. Wang, *ICASSP, IEEE International Conference on Acoustics, Speech and Signal Processing - Proceedings*, pp. 5764–5767, 2011.
[2] L. Chen *et al.*, *Medical Physics*, vol. 35, no. 8, pp. 3482–3490, 2008.
[3] R. Chityala *et al.*, vol. 5745, no. 1, apr 2005, p. 583.
[4] D. Kolditz *et al.*, *Medical Physics*, vol. 37, no. 6, pp. 2719–2730, 2010.
[5] E. Pearson *et al.*, *Journal of X-Ray Science and Technology*, vol. 24, no. 3, pp. 361–377, jun 2016.
[6] J. W. Stayman *et al.*, in *Proc SPIE Int Soc Opt Eng*, vol. 28, no. 10, mar 2016, p. 97830X.
[7] M. Defrise *et al.*, *Inverse Problems*, vol. 22, no. 3, pp. 1037–1053, 2006.
[8] G. J. Gang *et al.*, in *International Conference on Image Formation in X-Ray Computed Tomography*, 2018, p. (submitted).
[9] S. Zhao *et al.*, *Journal of X-Ray Science and Technology*, vol. 19, no. 2, pp. 155–172, 2011.
[10] A. J. Mathews *et al.*, *SPIE Medical Imaging (accepted paper)*, no. March 2017, pp. MI101–361, 2017.
[11] A. Sisniega *et al.*, *Medical Physics*, vol. 40, no. 5, pp. 1–19, 2013.
[12] L. Li *et al.*, *Journal of X-Ray Science and Technology*, vol. 17, no. 2, pp. 135–152, 2009.
[13] H. Yu and G. Wang, *Physics in Medicine and Biology*, vol. 54, no. 9, pp. 2791–2805, 2009.
[14] S. Bartolac *et al.*, *Medical Physics*, vol. 38, no. SUPPL.1, 2011.